Volume 18
Number 15
23 April 2026
Pages 7811-8388

Nanoscale

rsc.li/nanoscale

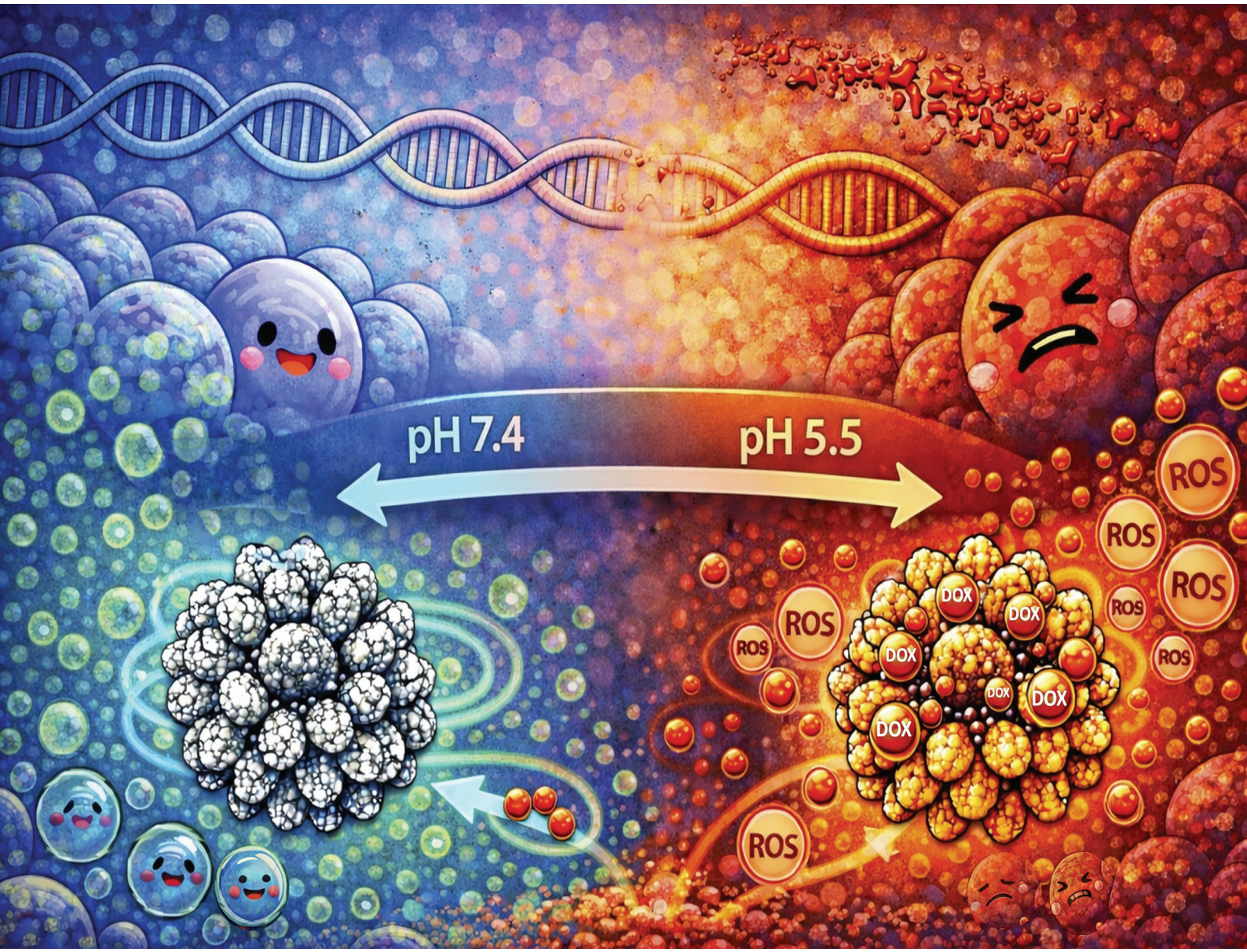

ISSN 2040-3372

ROYAL SOCIETY OF CHEMISTRY

PAPER
Nguyen Thi Kim Thanh *et al.*
Smart pH-responsive magnetic iron oxide nanoflower–chitosan nanogels for controlled drug delivery in cancer therapy

NCNST

Nanoscale

PAPER

View Article Online
View Journal | View Issue

Cite this: *Nanoscale*, 2026, **18**, 8041

Smart pH-responsive magnetic iron oxide nanoflower–chitosan nanogels for controlled drug delivery in cancer therapy

Bengi Ozkahraman, †[a,b,c] Liudmyla Storozhuk, †[b,c] Dongdong Guo,[b,c] Le Duc Tung,[b,c] Stefanos Mourdikoudis [b,c] and Nguyen Thi Kim Thanh *[b,c]

There has been a recent surge in the development of drug delivery systems that are specifically targeted towards tumors. The primary objective of these systems is to enhance the efficacy of anti-tumor drugs while simultaneously reducing any potential harmful side effects. This study focuses on designing a surface coating that is pH-responsive for iron oxide nanoflower (IONF) cores, allowing the controlled release of the drug doxorubicin (DOX). To achieve this, IONFs were coated with chitosan (CS) using NaOH, tripolyphosphate (TPP), and glutaraldehyde (GLU) as crosslinking agents. XRD and FTIR techniques were utilized to confirm the structure of the CS-IONF particles and determine the physical interaction and chemical bonding. TEM imaging was used to examine the morphology of the prepared CS-covered IONFs and drug-loaded CS-covered IONFs. The pH-responsive nature of the particles was characterized using the dynamic light scattering (DLS) technique in different pH media (pH 4, 5.5, and 7.4). The results showed that the CS-coated IONF nanogels exhibited excellent controlled pH-responsive release profiles, with a higher release in a pH 4 medium. Moreover, the CS-coated IONF nanogels demonstrated a high DOX loading capacity and efficiency of 67.3 ± 5.7% and 84.1 ± 7.2%, respectively. The biocompatibility of the developed formulation was also investigated through the MTT assay, which revealed the safety of the formulation in biological systems. Finally, flow cytometry analysis was performed to evaluate the efficiency of the drug delivery system.

Received 11th November 2025,
Accepted 15th January 2026

DOI: 10.1039/d5nr04770f

rsc.li/nanoscale

1. Introduction

Cancer is a significant public health threat that has severe economic and psychological impacts on society and individuals at a global level.[1,2] As per current life-saving innovation, the standard scientific approaches for treating cancer include surgery, radiation therapy and chemotherapy. Chemotherapy has become widespread for treating solid tumors.[3] Unfortunately, conventional chemotherapy has severe adverse effects including poor selectivity towards cancer cells, a low drug accumulation concentration at the tumor targeting site, and the development of multidrug resistance in the patient's body.[4] Routine chemotherapy tends to have suboptimal effects, accompanied by severe toxic side effects on normal tissues due to the non-specific nature of chemotherapeutics. Drug delivery systems target cancer cells to address these challenges while minimising the impact on normal tissues. A promising strategy involves delivering drugs specifically to cancer cells in contrast to healthy tissue using drug delivery systems.[5] As tumor sites typically exhibit lower pH than healthy cells, developing pH-responsive systems could enhance the selectivity of anticancer drugs compared to conventional cancer treatments.[6,7] This approach aims to mitigate side effects (nausea, hair loss, infertility, neurotoxicity, poor immune response to infection, *etc.*) and eliminate the risk of overdose.[2,7] Furthermore, these systems can enhance drug accumulation in tumor sites by taking advantage of the increased permeability and retention effect (EPR).[8]

Conventional cancer treatment often fails, as the drug may not reach the target site with effective concentrations. A compelling alternative to traditional therapy involves targeted drug delivery utilising nanoparticles as smart carriers.[9,10] This allows specific delivery of drugs to the site of action, facilitating dose reduction and decreasing drug-associated toxicity.[11]

The development of drug delivery systems for the controlled release of drugs has received increasing attention. Nanocarriers, including liposomes, nanogels, dendrimers, and

[a]*Department of Chemical Engineering, Hitit University, Corum, 19030, Turkey*
[b]*UCL Healthcare Biomagnetics and Nanomaterials Laboratories, London, W1S 4BS, UK. E-mail: ntk.thanh@ucl.ac.uk*
[c]*Biophysic Group, Department of Physics and Astronomy, University College London, London WC1E 6BT, UK*
† These authors contributed equally to this work.

polymeric micelles, offer a good solution for targeted drug release and represent established options for deployment in drug delivery systems.[5] Nanoparticles possess advantageous properties, including the capacity for targeted delivery and high stability, rendering them appealing for drug delivery applications.[7] Magnetic nanoparticles belong to the next generation of drug carriers, leveraging their distinctive physicochemical characteristics.[12] These particles exhibit inherent features that enable non-invasive control of their destiny in various applications, such as magnetic separation, biosensors, gene delivery, magnetic resonance imaging, and magnetic fluid hyperthermia, among others.[13–16] Magnetic nanoparticles loaded with a drug enable a targeted delivery to a specific site, such as a location containing cancerous cells, while also providing an opportunity for simultaneous imaging using an applied localised magnetic field.[1,17] Multicore iron oxide nanoparticles, known as IONFs, can be synthesised *via* various methods, among which the polyol route is an exceptionally versatile and attractive approach due to its simplicity, controllability, and scalability.[18,19] Such particles offer notable benefits compared to single-core ones due to crystallographic continuity that fosters cooperative interactions, amplifying susceptibility and preserving superparamagnetic characteristics.[20]

Chitosan, a positively charged natural linear polysaccharide derived from the deacetylation of chitin, possesses the merits of good biocompatibility, biodegradability, and non-toxic properties.[21] Chitosan and iron oxide have been widely used in biomedical applications and are components of several FDA-approved products. Both chitosan (in certain medical applications) and iron oxide (*e.g.*, as MRI contrast agents) have been designated as GRAS (generally recognized as safe) or included in approved formulations, supporting their biocompatibility and potential translational relevance.[1,22–26] The amine ($-NH_2$) and hydroxyl (–OH) groups present in the CS backbone could react with various chemical moieties for structural modification.[15,27] This process enhances the versatility of CS, facilitating the development of functional polymers, and broadens its range of applications.[28] Additionally, the pH-responsive behaviour of CS is primarily attributed to the protonation of its amino groups in the backbone at different pH values.[11] Recently, much attention has been devoted to organic–inorganic hybrid nanoparticles aiming to optimise the performance of nanomaterials and the integration of magnetic particles into polymers. In this way, the resulting composites will simultaneously benefit from the characteristics of both constituting entities.[29,30]

The formation of a hydrogel depends on several factors, including the nature of the crosslinking agent, the concentration of chitosan, and the molecular weight distribution of the chitosan chains in solution. In our study, when crosslinking agents such as GLU, NaOH, and TPP were added, crosslinking occurred between the adsorbed chitosan layers. In the literature, TPP, a polyvalent anion with three negatively charged phosphate groups, facilitates the crosslinking of chitosan molecules by establishing strong electrostatic interactions with the positively charged amine groups. This ionic interaction promotes the formation of homogeneous polymer layers, resulting in a stable chitosan coating around the iron oxide nanoparticle core. As demonstrated in a published study, crosslinked chitosan gels can be removed from the system under specific conditions. This process is driven by electrostatic attraction forces between the phosphate groups of TPP and the amine groups on chitosan, enabling the nanoparticles to be coated with a biocompatible and stable layer.[31,32]

DOX is a clinically widely used chemical chemotherapeutic agent that prompts apoptosis in cancer cells.[33,34] The literature states that DOX is used to treat various cancers, such as breast, lung, and ovarian cancers.[35] As reported in an earlier study, DOX-loaded CS-coated iron oxide magnetic nanoparticles have great potential for targeted delivery[36,37] and imaging.[38] A simple design using pH-responsive CS-modified iron oxide nanoparticles for the release of DOX in ovarian cancer treatment was reported by Adimoolan *et al.*[36]

Herein, for the first time, we present a systematic study comparing several different crosslinking strategies using NaOH, TPP and GLU in order to be able to identify the optimum conditions for the best colloidal stability, pH-responsive drug release and suitable size for intratumoral injection. The CS-coated seed (sIONFs) (see section 2.2) and DOX-loaded CS-coated sIONFs were characterised using Fourier transform infrared spectroscopy (FTIR), DLS, and ζ-potential analysis. The morphological features of the synthesised nanocarriers were observed by transmission electron microscopy (TEM). The structure of CS-coated sIONFs was confirmed by X-ray diffraction (XRD). Besides, the entrapped efficiency and drug loading of DOX were quantified. The pH response of drug release from DOX-loaded nanoparticles was conducted at different pH values (4, 5.5, and 7.4). Furthermore, *in vitro* cell viability studies were carried out, which provided insight into the toxicity of the nanocarriers.

2. Materials and methods

2.1. Materials

CS (low molecular weight), fluorescein-5-isothiocyanate (FITC), phosphate buffered saline (PBS) and DOX were bought from Sigma-Aldrich, UK. Acetic acid, NaOH, TPP, and GLU (25% in H_2O) were obtained from Merck, UK. Cell Counting Kit-8 (CCK-8) and cellulose membrane dialysis tubing (MWCO = 12 kDa) were purchased from Sigma-Aldrich, USA. Dimethyl sulfoxide (DMSO) was supplied by Merck, Germany.

2.2. Optimisation of chitosan-coated seed iron oxide nanoflowers

Synthesis of IONFs with intrinsic magnetic properties was previously developed by the Thanh research group, with the whole process including the initial seeding and two subsequent growth steps.[18] In this work, we use the seed IONFs as the versatile platform for all other types of IONFs (with two or more growth steps). Both the seed nanoflowers and the fully grown

nanoflowers exhibit similar surface morphology, composition, and crystal structure, as they share the same flower-like aggregation of iron oxide nanocrystals. Their surfaces present comparable crystallographic facets and surface chemistry, ensuring consistent interactions with coating materials (such as chitosan) and similar physicochemical behaviour. This structural and chemical similarity allows seamless growth from the seeds to larger nanoflowers without altering the surface characteristics that are important for coating, functionalization, and biocompatibility. Briefly, superparamagnetic sIONFs were synthesized based on our previously reported protocol, with slight modifications. More specifically, sIONFs were prepared *via* a modified thermal decomposition method in triethylene glycol (TREG), using 0.07 M $Fe(acac)_3$ as the iron precursor. Polyacrylic acid (PAA) was added to the reaction mixture to induce a negative surface charge – facilitating subsequent chitosan adsorption – and to promote the formation of the characteristic flower-like morphology. The precursor solution was heated to 180 °C at a rate of 3 °C min^{-1}, then heated further to 280 °C at 5 °C min^{-1}, and maintained at this temperature for 30 min under magnetic stirring (500 rpm).[18] The sIONFs were freeze-dried and utilized in further studies. To achieve a pH-responsive coating, three different sIONFs coated with chitosan nanogels were synthesised using physical binding with NaOH or TPP and chemical binding with GLU as crosslinking agents.

2.2.1. Synthesis of sIONFs@CS-NaOH nanocarriers. Chitosan was added to the sIONF suspension under mildly acidic conditions (pH 4 or 5.5), where it is soluble and positively charged. Due to the electrostatic interaction between the negatively charged sIONF surface and the cationic chitosan chains, CS formed a uniform polymer layer around each nanoflower. Crosslinking agents (TPP, GLU, or NaOH) were subsequently used to stabilize the coating. CS-coated sIONFs were produced using previously reported methods with slight modifications.[37] In particular, a 0.5% w/v CS solution was dissolved in acetic acid (1% w/v). CS solution was then added to sIONFs (0.01 g) and homogeneously dispersed under vigorous stirring for 30 min at room temperature. Finally, the solution was magnetically stirred while 1 M NaOH was added dropwise for 10 min. After the reaction, CS-coated sIONFs (sIONFs@CS-NaOH) were extracted using an external magnet, washed with Milli-Q water multiple times, and dried overnight in a freeze-dryer.

2.2.2. Synthesis of sIONFs@CS-TPP nanocarriers. CS-coated sIONFs were produced using previously reported methods with slight modification using the ionic gelation technique (Scheme 1).[38] The first steps of synthesis are the same as described above. In the last step, the aqueous solution of TPP (0.1% w/v) was added dropwise to the solution under magnetic stirring for 15 min.

2.2.3. Synthesis of sIONFs@CS-GLU. GLU solution (0.3 mL) was added dropwise to the CS-coated sIONF solution under magnetic stirring for 30 min.[39] CS-sIONFs@CS-GLU was separated from the reaction mixture, washed and dried as described in 2.2.1.

2.3. Characterisation

2.3.1. Structure and particle size analysis. The structural properties of the samples were characterised using an FTIR spectrophotometer (PerkinElmer, USA) in the range of 4000–600 cm^{-1}. The crystallinity of the synthesised samples was determined by XRD. The diffraction patterns of the samples were recorded over a Bragg angle range from 20° to 100° (PANalytical X'Pert3 diffractometer, Malvern Instruments). sIONFs and modified sIONFs were characterised using a Zetasizer Nano ZS (Malvern Instruments, UK). Before conducting DLS measurements, the samples were filtered through a

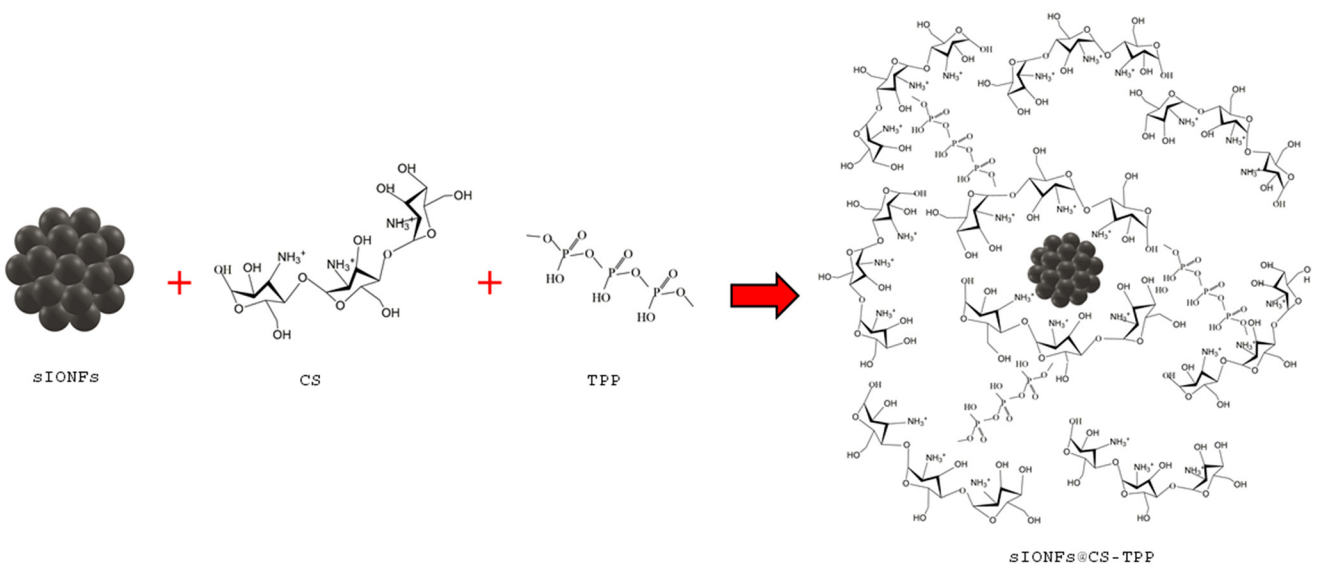

Scheme 1 Schematic illustration of sIONFs@CS-TPP synthesis yielding biocompatible particles for cancer treatment.

0.45 μm syringe filter and sonicated for 5 min. To determine the pH responsiveness of the CS-coated sIONFs, the samples were investigated with different pH values (4, 5.5, and 7.4) by DLS analysis.[27]

2.3.2. Morphological characterisation. TEM imaging was performed using a JEM 1200-EX, JEOL Ltd (Japan) microscope. Diluted aqueous dispersions of particles were drop-cast onto carbon-coated copper grids and allowed to dry in air. The grids were examined by TEM at an accelerating voltage of 120 kV at different magnifications. By utilizing TEM images at varying magnifications and ImageJ image analysis software, we were able to carry out an accurate and comprehensive particle size analysis.[18]

2.3.3. Thermogravimetric analysis. Thermogravimetric analysis (TGA) was conducted to determine the amount of sIONFs in the samples indirectly, *via* the identification of the organic mass of the samples. It was conducted in a controlled environment under a nitrogen gas atmosphere using a Discovery TGA analyser manufactured by TA Instruments. The samples were subjected to a gradual temperature increase from ambient temperature to over 700 °C at a constant rate of 10 °C min^{-1}.

2.3.4. Magnetic properties. The magnetic properties of sIONFs were analyzed by obtaining M–H plots using applied fields of up to 50 kOe. Additionally, zero-field-cooled (ZFC) and field-cooled (FC) magnetization *versus* temperature measurements were performed (from 300 K to 5 K) at 100 Oe using an MPMS-5S superconducting quantum interference device (SQUID) magnetometer (Quantum Design UK and Ireland Ltd).

2.3.5. Magnetic heating efficiency. AC magnetometry was employed to measure dynamic hysteresis loops with low field parameters. The measurement was carried out using pick-up coil technology with the AC Hyster™ setup provided by NanoTech Solutions (Madrid, Spain). The suspension used for the measurement consisted of 40 μL of sIONF aliquot.

To calculate the specific absorption rate (SAR), we used the area (A) enclosed by the hysteresis loops, multiplied it by the number of loops per second (frequency), and then normalized it by the sample concentration (mass per unit volume of the colloidal sample) (eqn (1)).[40]

$$\mathrm{SAR}\left(W_g^{-1}\right) = \frac{f}{c}A = \frac{f}{c}\mu_0 \oint M\,\mathrm{d}H \quad (1)$$

2.4. Drug loading and releasing

The loading procedure was adapted from a previous study.[41] In this procedure, sIONFs@CS-TPP (1.5 mg mL^{-1}) was dispersed in a PBS medium containing a concentration of DOX (0.1 mg mL^{-1}) and mixed and stirred at room temperature for 24 h to allow passive diffusion and adsorption of the drug onto the chitosan coating. After incubation, excess unbound DOX was removed by magnetic separation of sIONFs and washing. The studies were conducted three times to ensure accuracy. The loading capacity and loading efficiency were calculated according to eqn (2) and (3), respectively:[9]

$$\text{Loading capacity } \% = \frac{\text{Initial drug amount in formulation} - \text{Unentrapped drug}}{\text{Total weight of nanogels}} \times 100 \quad (2)$$

$$\text{Loading efficiency} = \frac{\text{Mass of drug in nanogel}}{\text{Mass of drug fed initially}} \times 100 \quad (3)$$

The effect of pH on the release profile of DOX was determined under different pH conditions, which simulate the tumor microenvironment and physiological medium. DOX-loaded sIONFs@CS-TPP was placed inside a dialysis bag with a molecular weight cut-off of 3500 Da and incubated at 37 °C with gentle shaking in the pH 4, 5.5, and 7.4 media. At each time interval, 1 mL of the release medium was extracted and replaced with fresh medium to retain a constant volume. Finally, the drug concentration of DOX was evaluated by UV spectrophotometry, as mentioned above. The release studies were conducted three times to secure accuracy and repeatability.

2.5. Fluorescent labelling of sIONFs@CS-TPP-DOX

An *in vitro* cellular uptake study of sIONFs@CS-TPP-DOX was performed using FITC-labelled nanoparticles.[42] Briefly, 4.2 mg of FITC was dissolved in 1 mL of DMSO and added to 20 mL of a 120 mg drug-loaded nanogel suspension for 6 h under dark conditions. The excess amount of FITC was removed by centrifugation thrice.

2.6. *In vitro* cellular uptake assay

In the confocal fluorescence microscopy observation experiment, the synthesised nanoparticles delivering DOX into prostate cancer PC3 and melanoma DX3 cells were visualised *via* the red fluorescence emitted by DOX. In brief, 5×10^4 cells were seeded onto 13 mm cell glass slides and incubated in a cell culture incubator at 37 °C with 5% CO_2 for 20 h. Subsequently, the old culture medium was replaced, and the cells were cultured for an additional 24 h in a fresh medium containing sIONFs@CS-TPP-DOX nanoparticles and DOX at a concentration of 50 μg ml^{-1}. Following this, the cells were stained with DAPI to label the cell nuclei, and their fluorescence behaviour was observed under a Leica DMI6000B. All fluorescence images were obtained under identical imaging settings, ensuring consistency and comparability across samples. The fluorescence signal was consistently detectable above background levels and sufficient to confirm the presence and spatial distribution of DOX within the nanoparticle formulations.[43,44]

2.7. *In vitro* cytotoxicity assay

The cytotoxicity of the synthesised nanoparticles, sIONFs@CS-TPP and sIONFs@CS-TPP-DOX, was tested by the CCK-8 assay on two cancer cell lines: PC3 and DX3. First, the PC3 and DX3 cells were seeded into 96-well plates with a density of 1×10^4 cells per well and incubated at 37 °C, 5% CO_2 for 12 h separately. Next, the old medium was replaced with fresh medium

containing various concentrations (2, 10, 50, 100, 500, and 1000 g mL^{-1}) of magnetic nanoparticles. After incubating at 37 °C for 24 h, the medium was removed and 100 μL of fresh medium containing 10% CCK-8 working solution was added per well. After 1 h incubation, the cells in 96-well plates were subjected to optical density measurement at 450 nm (OD 450 nm).

3. Results and discussion

3.1. Characterisation studies of sIONFs@CS-TPP and sIONFs@CS-TPP-DOX

The synthesis of the CS-coated sIONFs is illustrated in Scheme 1. CS is water-soluble and positively charged under mildly acidic conditions, and it readily adsorbs onto the negatively charged surface of the sIONFs, which are functionalized with PAA. This electrostatic attraction facilitates the formation of a core–shell structure, rather than a bulk chitosan hydrogel. Each crosslinker acts through a distinct mechanism. TPP, a multivalent anionic crosslinker, interacts ionically with the protonated amine groups of chitosan, forming a physically crosslinked network through electrostatic interactions. GLU, on the other hand, forms covalent bonds between aldehyde groups and the free amino groups of chitosan, producing a more rigid and chemically stable network. In contrast, NaOH promotes gelation through deprotonation of chitosan chains, leading to partial precipitation and physical entanglement of polymer chains around the nanoparticle surface.

Together, these crosslinking strategies provide coatings with different stabilities and pH responsiveness, allowing fine control over drug loading and release properties. The FTIR spectrum of Fe_3O_4 shows characteristic peaks at 582 cm^{-1} and 3400 cm^{-1} attributed to the Fe–O stretching vibration and surface –OH groups (hydroxyl groups), respectively (Fig. 1a).[45] The FTIR spectrum of pure CS shows broad bands at 3200–3500 cm^{-1} and 2933 cm^{-1} corresponding to N–H (amide II) and O–H (hydroxyl group) stretching vibrations and $–CH_2$ (methyl group) stretching.[46] Due to the existence of free amines in the CS polysaccharide, weak absorption peaks are observed at 1658 cm^{-1}. The peak observed at 1044 cm^{-1} is attributed to the backbone structure of the CS molecule.[47] In the spectrum of sIONFs@CS-NaOH, the peak at 3347 cm^{-1} is assigned to the O–H (hydroxyl group) band. Moreover, the peaks at 1658 cm^{-1} and 885 cm^{-1}, which were related to NaOH in the well-synthesised coating, are also observed. The main functional groups of the CS structure at 1452 cm^{-1} and 1100 cm^{-1} can be ascribed to the N–H stretching vibration and C–O–C symmetric stretching, respectively.[48] The FTIR spectrum of sIONFs@CS-TPP shows characteristic bands, confirming the interaction between the amino groups of chitosan and the phosphate groups of TPP. The amide I band is observed at approximately 1634 cm^{-1}, corresponding to the C=O stretching vibrations of the chitosan amide groups. Additionally, the band at around 1071 cm^{-1} is due to the P–O stretching vibrations from TPP, indicating successful crosslinking.[49] The spectrum of sIONFs@CS-GLU was compared with that of CS. The absorption band at around 1580 cm^{-1}, which can be attributed to the bending vibration of $–NH_2$ groups, is often used as an indicator of crosslinking between chitosan and glutaraldehyde. However, this peak was not clearly observed in our spectrum. Instead, evidence for crosslinking was inferred from changes in the amide I region and other physicochemical properties of the particles, such as increased stability.[50]

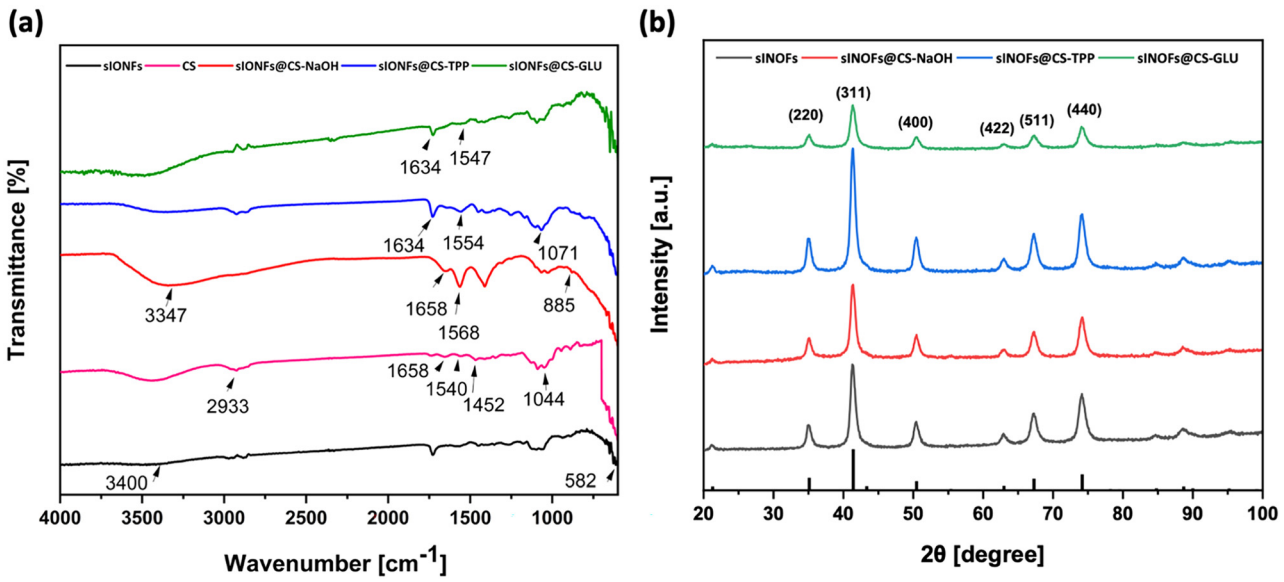

Fig. 1 (a) FTIR spectra of sIONFs, CS, sIONFs@CS-NaOH, sIONFs@CS-TPP and sIONFs@CS-GLU in the range of 4000–600 cm^{-1} and (b) XRD patterns of sIONFs, sIONFs@CS-NaOH, sIONFs@CS-TPP, and sIONFs@CS-GLU in the range of 20–100 (2θ, deg). The lines at the bottom display the positions of peaks and relative intensities corresponding to magnetite (JCPDS card 03-065-3107).

Moreover, the spectrum of sIONFs@CS-GLU shows absorption at 1734 cm^{-1}, which can be assigned to the C═O stretching vibration of amide groups and the C═N stretching vibration (Schiff base) of GLU.[51] Overall, in the spectra of sIONFs@CS-NaOH, sIONFs@CS-TPP, and sIONFs@CS-GLU, the characteristic N–H bending peak of the CS backbone at 1575 cm^{-1} shifted to 1568 cm^{-1}, 1554 cm^{-1} and 1547 cm^{-1}, respectively, due to the formation of an electrostatic bond between the negatively charged iron oxide and CS.[52,53] XRD measurements were performed to investigate the crystal structures of sIONFs, sIONFs@CS-NaOH, sIONFs@CS-TPP, and sIONFs@CS-GLU. As shown in Fig. 1b, the characteristic diffraction peaks for sIONFs at 2θ = 34.2°, 41.4°, 50.3°, 62.4°, 67.3°, and 73.4° correspond to the (220), (311), (400), (422), (511) and (440) crystal planes of Fe_3O_4, respectively (JCPDS card 03-065-3107).[18,51] In addition, the XRD patterns of sIONFs coated with CS (sIONFs@CS-NaOH, sIONFs@CS-TPP, and sIONFs@CS-GLU) appeared to be sharp and clear, which corresponded to the crystalline phase of Fe_3O_4 particles. This confirms that the CS coating did not affect the crystal structure of Fe_3O_4 magnetic particles.[29,47] A comparison of the FTIR spectra of the sIONFs@CS-TPP nanocarriers and DOX loaded sIONFs@CS-TPP-DOX is depicted in Fig. 2a. According to previous reports, the spectrum of pure DOX shows a broad peak at about 3506 cm^{-1}, a peak at 1734 cm^{-1}, and another peak at 1582 cm^{-1}, which are associated with the stretching of phenolic O–H groups, carbonyl group stretching vibration and C═C bond vibrations of the aromatic rings, respectively.[54] In the FTIR spectrum of CS-sIONFs@TPP before DOX loading, bands near 1582 cm^{-1} and 1734 cm^{-1} are observed, which may be due to aromatic C═C stretching and carbonyl stretching vibrations, respectively. These bands partially overlap with characteristic DOX peaks, complicating exclusive assignment to DOX after loading. In the DOX-loaded samples, changes in intensity and peak shape were noted, supporting DOX incorporation. After loading DOX onto sIONFs@CS-TPP-DOX, changes in peak intensity were observed at 1547 cm^{-1} and 1734 cm^{-1}, attributed to the aromatic C═C stretching vibration and ketone group stretching bands of DOX, accompanied by a noticeable decrease in intensity.[55]

These bands partially overlap with characteristic DOX peaks, complicating exclusive assignment to DOX after loading. In the DOX-loaded samples, changes in the intensity and peak shape were noted, supporting DOX incorporation. The successful loading of DOX onto sIONFs@CS-TPP nanocarriers is corroborated by the presence of these peaks in the FTIR spectra. Among the formulations studied, sIONFs@CS-TPP exhibited a hydrodynamic size of <115 nm at pH 4 and 5.5, and approximately 181 nm at pH 7.4, which lie within the acceptable size range (10–200 nm) for prolonged circulation and reduced renal or hepatic clearance.[56,57] In the case of hydrophilic nanoparticles, their hydrodynamic size (d_{DLS}) in aqueous environments may be considerably larger than d_{TEM}, which measures the core size of NPs.[58] This is due to the surrounding layer of solvent molecules and ions that diffuse with NPs in solution.

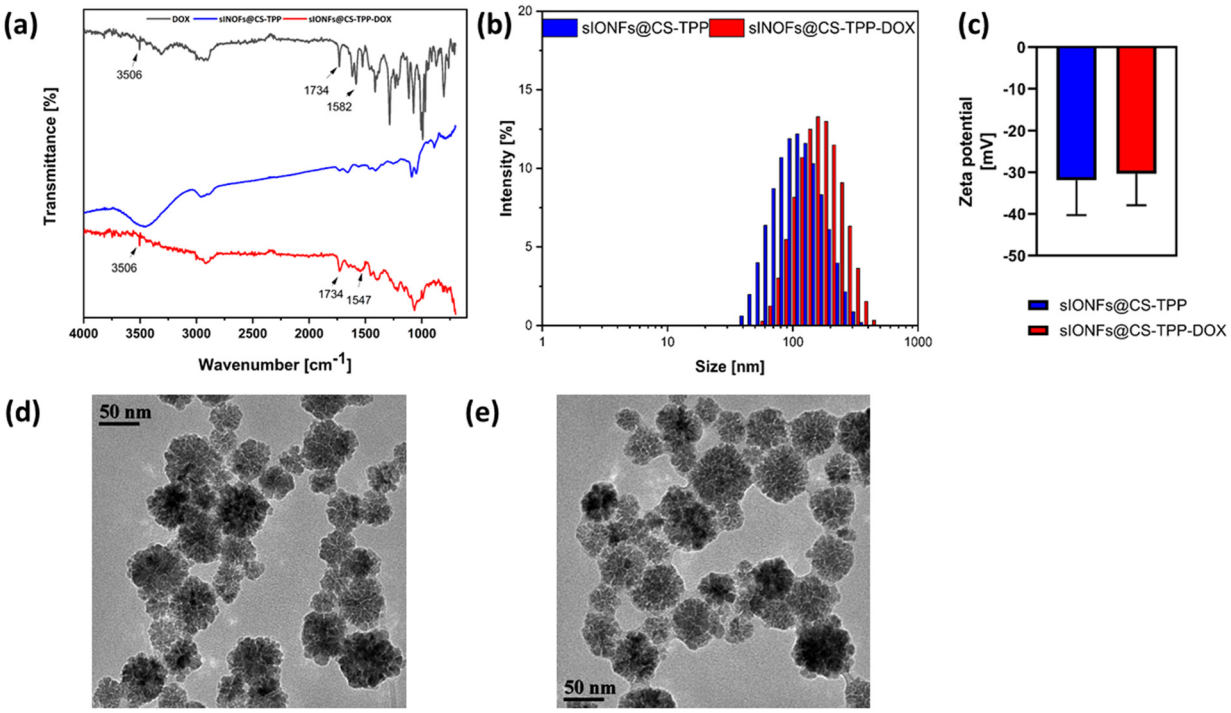

Fig. 2 (a) FTIR spectra of DOX, sIONFs@CS-TPP and sIONFs@CS-TPP-DOX in the range of 4000–600 cm^{-1}; (b) DLS diagram of sIONFs@CS-TPP and sIONFs@CS-TPP-DOX; (c) ζ-potential of sIONFs@CS-TPP and sIONFs@CS-TPP-DOX; and TEM images of (d) sIONFs@CS-TPP and (e) sIONFs@CS-TPP-DOX (scale bar: 50 nm).

However, as shown in Table S1, other formulations (*e.g.*, those prepared using NaOH or GLU) resulted in significantly larger particle sizes, in some cases approaching or exceeding 1 μm. Therefore, only the optimized sIONFs@CS-TPP sample was selected for further evaluation and is considered potentially viable for *in vivo* applications.

Furthermore, beyond electrostatic stabilization, steric hindrance provided by polymer coatings also contributes to the colloidal stability of the system. The presence of chitosan on the surface of sIONFs affects the ζ-potential changes too. The chitosan layer is known to be pH-sensitive, with protonation of amino groups occurring at lower pH, which boosts the positive charge. However, as the pH increases, chitosan's isoelectric point is reached, and the surface charge becomes more negative, as observed in the ζ-potential measurements. The average size and ζ-potential were employed to evaluate the hydrodynamic size and surface charge of the sIONFs@CS-TPP and sIONFs@CS-TPP-DOX nanocarriers in pH 5.5 buffer solution, as illustrated in Fig. 2b and c, respectively. As shown in Fig. 2b, the synthesised sIONFs@CS-TPP possessed a mean particle size of 114.4 ± 1.5 nm, while sIONFs@CS-TPP-DOX had an average size of 125.8 ± 2.9 nm. The incorporation of DOX into sIONFs@CS-TPP resulted in a slight growth in the hydrodynamic diameter of the nanocarriers. Additionally, the negative ζ-potential of the sIFs@CS-TPP-DOX particles reduced to −30.3 ± 8.4 mV compared to that of the sIFs@CS-TPP particles (−31.9 ± 8.4 mV) (Fig. 2c). Notably, the addition of DOX to these particles slightly affected their ζ-potential, but it remained within an acceptable range.[59] Several factors can cause the net ζ-potential of the CS-coated sIONFs to appear negative, even though CS remains as the outer shell. After CS adsorption, crosslinking (with TPP, GLU, or NaOH) can consume or neutralize the protonated amine groups ($-NH_3^+$) on CS. TPP introduces negatively charged phosphate groups, which can dominate the surface charge. NaOH treatment increases pH and deprotonates amino groups ($-NH_2$ instead of $-NH_3^+$), thereby reducing the positive charge. Glutaraldehyde crosslinking forms neutral Schiff bases (C═N), also decreasing the positive surface charge. As a result, the outer surface of the coated particle can become neutral or even negative, depending on the crosslinking route. TEM analysis helped to visualize the particle morphology. The TEM images of sIONFs@CS-TPP and sIONFs@CS-TPP-DOX are presented in Fig. 2d and e. The diameters of the sIONFs@CS-TPP and sIONFs@CS-TPP-DOX nanoparticles were found to be 49.1 ± 8.2 and 57.6 ± 11.5 nm (SI, Fig. S2 and Table S2), indicating successful synthesis and loading of the DOX nanocarriers.

It is possible that some CS-crosslinked hydrogel could be formed when NaOH, TPP or GLU was added to the solution. However, a low concentration of CS was utilized with an appropriate ratio between CS and sIONFs in order to ensure coating on sIONFs. Moreover, after the reaction, a magnet was employed to collect exclusively the CS-coated sIONFs; in this way, any CS-crosslinked hydrogel that might have been formed was safely discarded. Also, a low local concentration and reduced mobility of chitosan chains on the surface of sIONFs, along with possible steric hindrance from the nanoparticle core, prevented the formation of a continuous, cross-linked chitosan-sIONF gel network. This is supported by the TEM images (Fig. 2d and e), which clearly show a uniform coating and the absence of aggregated gel structures. Moreover, the sIONFs@CS-TPP and sIONFs@CS-TPP-DOX flower shapes provide a higher surface area, which assists in binding the maximum amount of drug, thereby enhancing the drug delivery efficiency.[60] The size differences obtained between TEM and DLS analyses can be attributed to the fact that TEM imaging is performed in the solid state.[61] In contrast, the D_h from DLS is measured in solution, incorporating the hydration layer, and is affected by surface charge, density, and solvent properties.[62] Similar observations have been reported in previous research on polymer-coated magnetic nanoparticles for drug delivery systems.[55] Mass loss at specific temperatures was used to determine the amounts of organic matter and iron oxide in the samples.

The TGA curves in Fig. 3 demonstrate a weight loss of around 2.1% for sIONFs, 0.9% for sIONFs@CS-TPP, and 1.7% for sIONFs@CS-TPP-DOX at a temperature of around 100 °C. This weight reduction could be due to eliminating OH groups and water molecules on the surface of sIONFs. Solvent evaporation is responsible for a weight loss of about 4% for sIONFs, 5% for sIONFs@CS-TPP, and 6.2% for sIONFs@CS-TPP-DOX in the temperature range of 200–250 °C. In the temperature range of 250–500 °C, the weight loss is primarily related to the decomposition of PAA and CS coatings. The PAA/CS-coated nanoparticles show total weight losses of 30.5% (sIONFs@CS-TPP) and 31.9% (sIONFs@CS-TPP-DOX) compared to that of the bare sIONFs (13.9%). This indicates the presence of a CS coating and DOX on the surfaces of sIONFs@CS-TPP and sIONFs@CS-TPP-DOX. After 500 °C, no weight loss is observed in the temperature range of up to 700 °C (Fig. 5), indicating the complete decomposition of the coated polymers. Finally, the residual weight corresponds to 86.1%, 69.5%, and 63.4% for sIONFs, sIONFs@CS-TPP, and sIONFs@CS-TPP-DOX, respectively.

3.2. Magnetic properties of sIONFs

Fig. 3b presents the hysteresis loops of sIONF samples before and after modification by CS and drug conjugation. By comparing the magnetic hysteresis curves before and after modification, it was found that all samples are superparamagnetic, and the modifications did not significantly affect the magnetic properties of the particles. The sIONFs, sIONFs@CS-TPP and sIONFs@CS-TPP-DOX showed coercivities of 30.1, 16.8 and 14.6 Oe and saturation magnetisation values of 79.3, 73.5 and 75.9 emu g_{IONPs}^{-1}, respectively. The specific loss power was determined by measuring the rate of temperature increase in the dispersion when exposed to an AC magnetic field. The SARs of the sIONFs, sIONFs@CS-TPP and sIONFs@CS-TPP-DOX samples were 1234.8, 1274.3 and 1224.3 W g_{Fe}^{-1} (ILP = 4.67, 3.88 and 4.24 nH m^2 kg_{Fe}^{-1}), respectively (Fig. 3c). Following the modification and drug conjugation, the analysis of the SAR and ILP values revealed a minor decrease in the

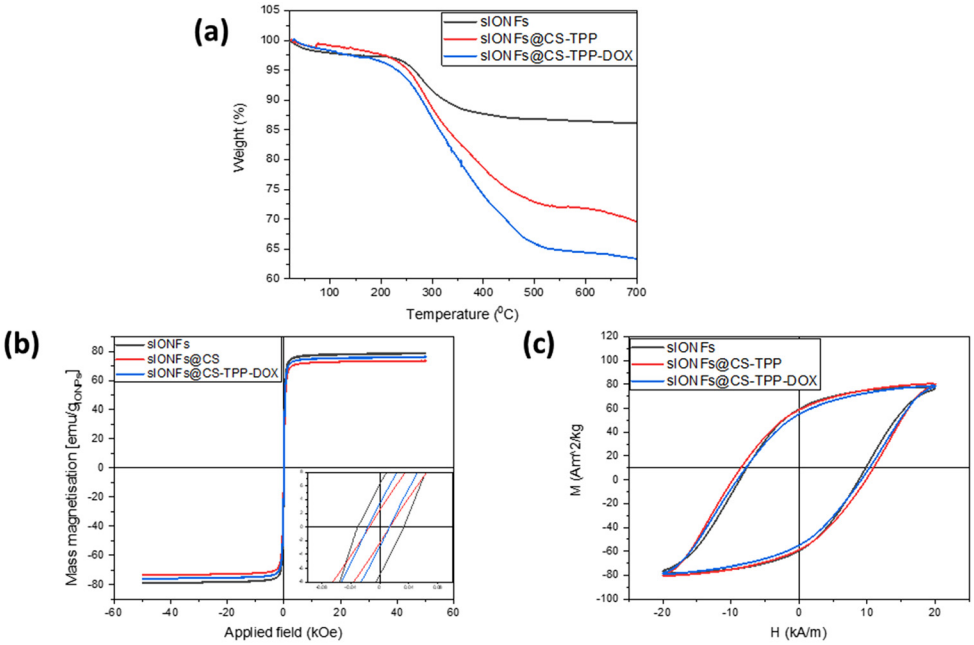

Fig. 3 (a) Thermogravimetric analysis curves of sIONFs, sIONFs@CS-TPP and sIONFs@CS-TPP-DOX. (b) Hysteresis curves of sIONFs, sIONFs@CS-TPP, and sIONFs@CS-TPP-DOX samples measured at 300 K. The inset shows the magnified hysteresis loops at low field strengths. (c) AC hysteresis loops of sIONFs, sIONFs@CS-TPP and sIONFs@CS-TPP-DOX samples recorded at room temperature and a magnetic field of 20 kA m^{-1} at 350 kH.

heating ability of the samples. These results indicate that the structural and chemical changes implemented during the modification process may have slightly impacted the heating capacity of the samples.

3.3. Particle size analysis and pH-responsive assessment

The particle size of nanocarriers plays a crucial role in clinical applications, with a particular focus on chemoprevention and chemotherapy using nanoparticles for local drug carriers.[63] In addition, the D_h of the coated samples was measured in a different medium to obtain information on pH-responsive behaviours. As shown in Table S1, sIONFs@CS-TPP was made up of particle sizes in the range of 80–180 nm.

Based on the literature, it has been found that sIONFs@CS-TPP possesses a particle size value that is suitable for drug delivery systems under all pH conditions. This implies that the drug release properties can be effectively controlled by modifying the pH of the environment. This makes such particles well-suited for drug delivery applications where targeted release is desired.

At the same time, CS is negatively charged at a physiological pH but positively charged under acidic conditions inside tumor cells. The sIONFs@CS-TPP particles show stability at physiology pH, and their small size allows for prolonged circulation in the body, making them suitable for effective drug delivery.[64,65]

The thickness of the CS coating was modulated by adjusting the CS concentration, reaction time, and crosslinker to CS ratio. We confirmed successful coating and estimated relative thickness using TEM/DLS/TGA (see Fig. 2b, d, e, and 3a and Tables S1–3).

The DLS size of the chitosan-coated nanoparticles changes with pH, due to aggregation and colloidal stability effects, rather than from the changes in the individual particle core size.

ζ-potential provides an assessment of the colloidal stability of the nanoparticles. Generally, nanoparticles exhibit high particle stability when their ζ-potential is above 30 mV (*i.e.*, its absolute value).[29] The ζ-potential of the CS-coated sIONFs is summarised in Table S1. It can be observed that the ζ-potential measurements of sIONFs@CS-TPP revealed a mean value of −31.9 ± 8.38 mV. Chitosan binds to sIONFs-PAA through electrostatic attraction, as well as hydrogen bonding and van der Waals interactions. Native chitosan, being a cationic polymer due to its primary amine groups, typically imparts a positive charge under acidic to neutral pH conditions. However, in our case, the observed negative ζ-potential of some CS-coated nanoparticles can be attributed to multiple factors: surface adsorption of counterions and the amine groups of CS that were consumed in the reaction with TPP and GLU. The observed negative ζ-potential of chitosan-coated NPs may also partially come from incompletely neutralized PAA groups remaining on the sIONF surface. This approach enabled the formation of a stable, uniform CS shell with desired surface properties. Our results are consistent with previous studies on chitosan-coated nanoparticles.[66–68] A high value of the ζ-potential confirms the excellent stability of the nanocarrier, as reported in the literature.[67,68] According to the

properties and advantages mentioned above, sIONFs@CS-TPP was deemed to have the best ability to improve the nano-drug carrier system.

Additionally, the pH sensitive CS layer contributes to the ζ-potential alterations, with protonation of amino groups at lower pH increasing the positive charge, while at higher pH, the surface charge becomes more negative, aligning with the isoelectric point of CS.[69]

As a chemo-therapeutic agent, DOX was loaded into sIONFs@CS-TPP-DOX nanocarriers by a co-assembly method.[31] The DOX loading capacity and efficiency in the nanocarrier were estimated according to eqn (1) and (2) and were 67.3 ± 5.7% and 84.1 ± 7.2%, respectively. Moreover, the carrier and the chemical composition of the drug play a crucial role in determining the drug loading capacity.[70]

While each component of sIONFs offers negligible drug-loading capacity due to their dense structure, their unique flower-like morphology provides a significantly larger surface area compared to conventional spherical nanoparticles. This increased surface area enhances loading capacity and consequently increases the amount of DOX retained in the CS-TPP matrix. The coating forms a thin layer (see Fig. 2d and e), and DOX retention is likely facilitated by a combination of electrostatic interactions (between positively charged DOX and the anionic CS-TPP matrix), hydrogen bonding, and hydrophobic interactions between them. Similar high loading capacities (≈67%) have been reported in the literature using comparable DOX loading approaches.[31,41,71]

The mechanism of drug loading for DOX most likely occurs through drug conjugation chemistry on the surfaces of CS-sIONFs. The FTIR spectra indicate that the strong hydrogen bonding interaction between the carboxylic groups in the nanoparticles and the hydroxyl groups in the drug structure contributes to the high drug loading capacity (Fig. 2a).[71]

3.4. Assessment of the pH-responsive profile of DOX release

To achieve pH-responsive drug release, DOX-loaded CS-sIONF nanocarriers were incubated at 37 °C. The electrostatic interactions between DOX and the CS-TPP matrix result in stronger drug retention compared to passive diffusion alone. While loading was performed after CS-coating formation, the process is not purely passive diffusion; instead, it leverages charge-mediated adsorption that leads to a more stable association of DOX with the particle surface.

DOX release profiles were determined using three different buffers at pH 7.4, 5.5 and 4, which represent the pH of blood, the pH of the acidic tumor microenvironment, and the pH of endo/lysosome, respectively.[72,73] The drug release profile results are presented in Fig. 4. The release of DOX was observed with 67.3 ± 20.3%, 51.8 ± 9.6%, and 28.3 ± 7.7% at pH 4, 5.5, and 7.4 after 24 h, respectively, which confirms the pH-sensitivity of the developed nanocarrier.

The release profile of DOX from sIONFs@CS-TPP shows a plateau of around 50% release after ~6 h, even under acidic conditions (pH 4 and 5.5). This can be attributed to the strong electrostatic and hydrogen-bonding interactions between DOX and the CS-TPP shell, which tightly retain a portion of the drug. At pH 4, chitosan is more protonated and swells more extensively, resulting in increased polymer chain mobility and larger diffusion pathways for DOX, accelerating release compared to pH 5.5. Even though the CS layer is thin, these differences in the protonation state and swelling behaviour are sufficient to modulate the release kinetics noticeably. Literature reports indicate that chitosan protonation occurs rapidly (within minutes) upon pH changes, and swelling typically reaches equilibrium within hours depending on cross-linking density and environmental conditions. These dynamics align with the release profiles observed in this study.[74–77] The initial burst release occurs due to the diffusion of DOX out of nanomatrices.[78] Moreover, the higher release of sIONFs@CS-TPP-DOX under acidic conditions could further facilitate the release of DOX in the tumor environment.[79,80] The enhanced DOX release in the tumor environment reduces off-target toxicity and tackles the limitations of conventional DOX chemotherapy.[11,78] These results revealed that the developed nanocarriers were pH-sensitive and highly responsive in the desired pH range, aligning with the previous literature and rendering them a promising candidate for a biological drug delivery system in cancer treatment.[30,35,81]

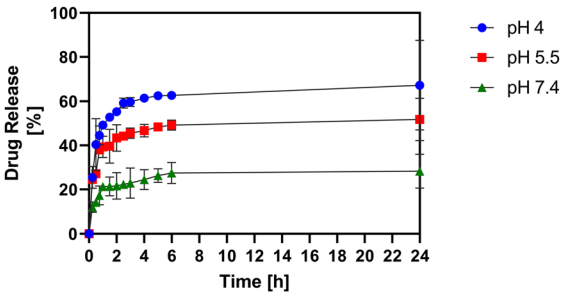

Fig. 4 *In vitro* drug release studies of sIONFs@CS-TPP-DOX in different pH media (mean values ± SD, n = 3).

Furthermore, our release studies indicate that the drug is not released at the same rate as it is loaded, supporting the role of electrostatic retention rather than simple diffusion. This is evident from the lag phase and sustained release profile observed in our *in vitro* release curves, which differ significantly from the loading kinetics.[31,41,71]

If nanoparticles are injected intravenously, they end up primarily in the liver and the spleen. Even with antibody conjugation, tumour targeting is <1%.[82] Therefore, the consensus in the scientific and medical community is that MH treatment would work best for direct intra-tumoral injection. It has the advantage that no other organs are affected and larger doses can be delivered to the targeted area. This design was chosen intentionally to explore the effects of chitosan's pH-responsive behaviour for drug loading and release in acidic tumors.

3.5. *In vitro* cellular uptake

To investigate the drug release profile of the synthesised sIONFs@CS-TPP nanoparticles within cells, sIONFs@CS-TPP-DOX was co-incubated with PC3 and DX3 cells for 24 h. As

shown in Fig. 5, the red fluorescence emitted, stimulated by intracellular DOX, is comparable in both PC3 and DX3 cells. It is observed that, compared to the unconstrained small-molecule chemotherapeutic drug DOX uptake on cells, the red fluorescence intensity emitted by cells treated with sIONFs@CS-TPP-DOX is nearly indistinguishable. This suggests that DOX loaded onto sIONFs@CS-TPP can be effectively delivered into the cells. Consistent with the results of the earlier drug release experiments, this finding substantiates the excellent drug carrier functionality of sIONFs@CS-TPP and its proficient drug delivery capabilities.

3.6. Cytotoxicity study

A cell counting assay was employed to assess the toxicity of the synthesised iron-based nanoparticles. Fig. 6 illustrates the viability of cells after treatment with nanoparticles at varying concentrations ranging from 2 to 1000 μg ml^{-1}. sIONFs@CS-TPP has minimal impact on cell viability, even at concentrations as high as 1000 μg ml^{-1}, indicating excellent biocompatibility in the absence of loaded DOX. However, upon loading DOX onto sIONFs@CS-TPP to form sIONFs@CS-TPP-DOX nanoparticles, cell growth is significantly inhibited. Specifically, for PC3 cells, at a concentration of 1000 μg ml^{-1} sIONFs@CS-TPP-DOX, 42.4 ± 9.8% of cells are killed. In contrast, DX3 cells are nearly entirely killed at this concentration.

Significantly, treatment of DX3 cells with 500 μg ml^{-1} of sIONFs@CS-TPP-DOX resulted in more than 95% cell killing, whereas the corresponding sIONFs@CS-TPP had no significant cell killing effect. Even at a lower 100 μg ml^{-1} concentration of sIONFs@CS-TPP-DOX, 58.85 ± 8.43% of DX3 cells

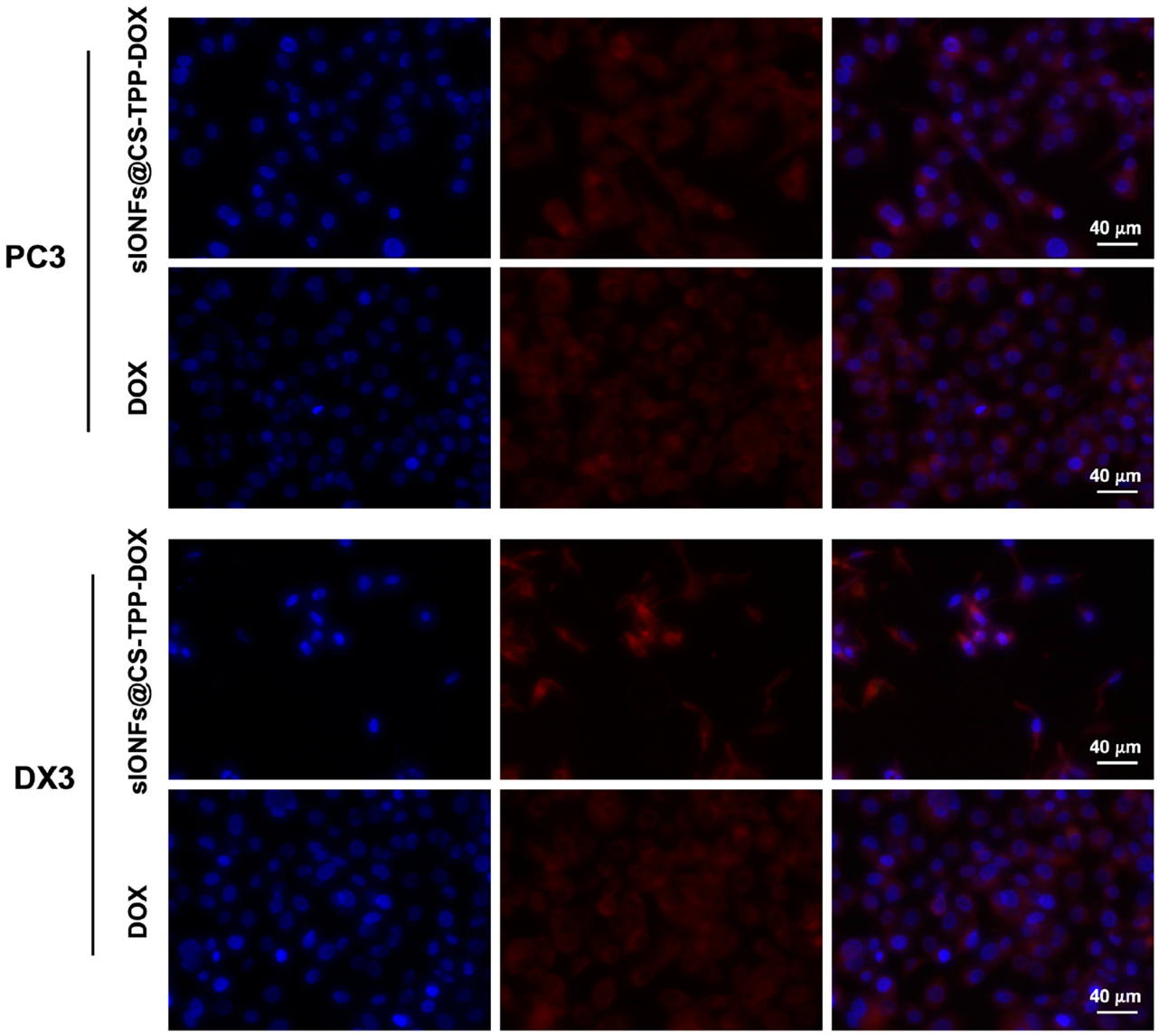

Fig. 5 Confocal fluorescence images of PC3 and DX3 after treatment with sIONFs@CS-TPP-DOX and DOX. Blue represents cell nuclei stained with DAPI; red represents intrinsic fluorescence from DOX and red/blue represents merged images (scale bar: 40 μm).

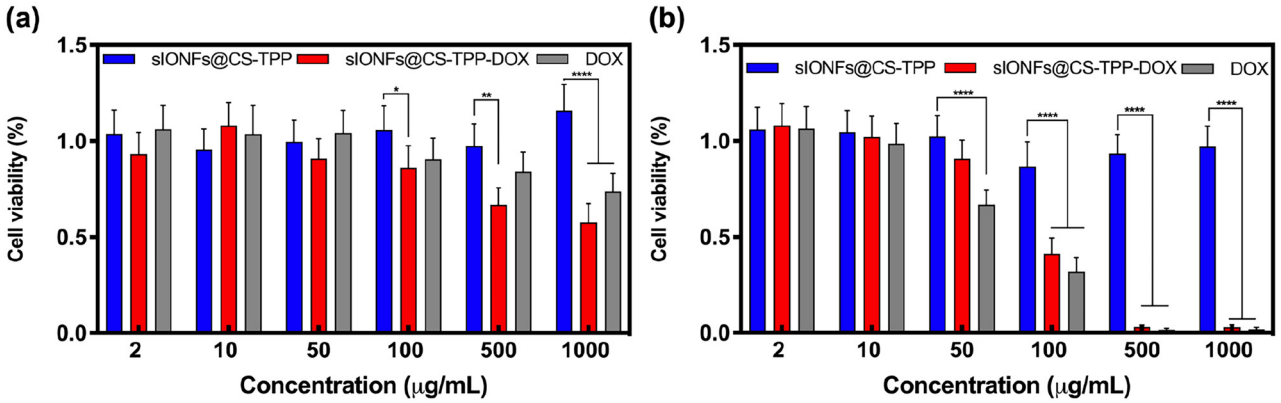

Fig. 6 Cell viability of PC3 (a) and DX3 (b) cells treated with sIONFs@CS-TPP, sIONFs@CS-TPP-DOX and DOX at various concentrations (2, 10, 50, 100, 500, and 1000 μg mL^{-1}) for 24 h exposure time. The results are presented as mean ± s.d., n = 4. Statistical analysis was performed using Student's t-test, and the significance is indicated as * $p < 0.05$, ** $p < 0.01$, *** $p < 0.001$, and **** $p < 0.0001$.

are eliminated. Overall, compared to sIONFs@CS-TPP, there is a significant difference in the DX3 cytotoxicity of free DOX and sIONFs@CS-TPP-DOX at concentrations of 100 μg ml^{-1}, 500 μg ml^{-1} and 1000 μg ml^{-1}. At these concentrations, sIONFs@CS-TPP-DOX exhibits comparable cytotoxicity to free DOX against DX3 cells and for PC3 cells, sIONFs@CS-TPP-DOX enhances toxicity, but not as much as in DX3 cells. It is suggested that the synthesized sIONFs@CS-TPP-DOX can provoke tumor suppression effects comparable to small molecule chemotherapy drugs (DOX). The observed differences in the lethal effect on PC3 and DX3 tumors may stem from inherent variations in the tolerance of prostate cancer and melanoma to both DOX and DOX conjugated with nanoparticles. Further investigation is still required to elucidate the relevant biological mechanisms.

Conclusions

An advanced drug delivery system has been successfully developed using nanogels based on pH-responsive CS-coated sIONFs and DOX. The synthesis process involved using both chemical and physical crosslinking agents to create the nanogels; the drug release is optimized in an acidic medium at 67.27 ± 20.35%. To evaluate the effectiveness of the drug delivery system, *in vitro* cytotoxicity studies of DOX-loaded sIONFs@CS-TPP nanogels were conducted on PC3 and DX3 cancer cell lines. The results demonstrated the efficient cellular uptake and a dose-dependent reduction in cell viability. Notably, sIONFs incorporated into CS-TPP polymeric particles without DOX loading exhibited excellent biocompatibility, showing no significant cytotoxicity even at 1000 μg mL^{-1}. The developed sIONFs@CS-TPP-DOX nanogels provide a platform for incorporating different drugs for different types of cancers. Overall, this study introduces a systematically optimized, multifunctional nanoplatform that overcomes key challenges in targeted cancer therapy and provides new insights into the design of pH responsive, injectable nanocarriers for future translational applications.

Author contributions

Bengi Ozkahraman: synthetic methodology, visualization, investigation, data curation, and writing – original draft. Liudmyla Storozhuk: characterisation methodology of nanoparticles, visualization, investigation, data curation, and writing – review and editing. Dongdong Guo: methodology for cellular work, visualization, investigation, and data curation. Le Duc Tung: characterisation of nanoparticles. Stefanos Mourdikoudis: writing – review & editing. Nguyen Thi Kim Thanh: conceptualization, critical data analysis, writing – review & editing, supervision and securing funding.

Conflicts of interest

There are no conflicts to declare.

Data availability

All data generated or analysed during this study are included in this published article and its supplementary information (SI). Supplementary information is available, containing additional TEM, DLS and SQUID characterization of chitosan-coated iron oxide NFs. See DOI: https://doi.org/10.1039/d5nr04770f.

Acknowledgements

Bengi Ozkahraman sincerely thanks the COST Action CA17140 "Cancer nanomedicine – from the bench to bedside" for financial support.

References

1 S. Siavashy, M. Soltani, F. Ghorbani-Bidkorbeh, N. Fallah, G. Farnam, S. A. Mortazavi, F. H. Shirazi, M. H. H. Tehrani and M. H. Hamedi, *Carbohydr. Polym.*, 2021, **265**, 118027.
2 A. Farokh, M. Pourmadadi, H. Rashedi, F. Yazdian and M. A. Navaei-Nigjeh, *Int. J. Biol. Macromol.*, 2023, **237**, 123937.
3 Z. Omrani, M. Pourmadadi, F. Yazdian and H. Rashedi, *Int. J. Biol. Macromol.*, 2023, **250**, 125897.
4 Y. Dong, R. Fu, J. Yang, P. Ma, L. Liang, Y. Mi and D. Fan, *Int. J. Nanomed.*, 2019, **14**, 6971.
5 M. Rajabzadeh-Khosroshahi, M. Pourmadadi, F. Yazdian, H. Rashedi, M. Navaei-Niggjeh and B. Rasekh, *J. Drug Delivery Sci. Technol.*, 2022, **74**, 103443.
6 P. Xie and P. Liu, *Carbohydr. Polym.*, 2020, **236**, 116093.
7 M. Pourmadadi, M. Ahmadi, M. Abdouss, F. Yazdian, H. Rashedi, M. Navaei-Nigjeh and Y. Hesari, *J. Drug Delivery Sci. Technol.*, 2022, **70**, 102849.
8 L. Beola, N. Iturrioz-Rodriguez, C. Pucci, R. Bertorelli and G. Ciofani, *ACS Nano*, 2023, **17**, 18441.
9 K. Kheiri, N. Sohrabi, R. Mohammadi and M. S. Amini-Fazl, *Int. J. Biol. Macromol.*, 2022, **202**, 191.
10 S. Khan, A. Madni, H. Shah, N. S. A. Jan, A. Basit, N. Rai, A. Ali and M. M. Khan, *Int. J. Biol. Macromol.*, 2022, **222**, 497.
11 R. Narayan, S. Gadag, S. P. Cheruku, A. M. Raichur, C. M. Day, S. Gard, S. Manandhar, K. S. R. Pai, A. Suresh, C. H. Mehta, Y. Nayak, N. Kumar and U. Y. Nayak, *Carbohydr. Polym.*, 2021, **261**, 117893.
12 R. P. Dhavale, R. P. Dhavale, S. C. Sahoo, P. Kollu, S. U. Jadhav, P. S. Patil, T. D. Dongale, A. D. Chougale and P. B. Patil, *J. Phys. Chem. Solids*, 2021, **148**, 109749.
13 Y. Ding, S. Z. Shen, H. Sun, K. Sun, F. Liu, Y. Qi and J. Yan, *Mater. Sci. Eng., C*, 2015, **48**, 487.
14 M. O. Besenhard, L. Panariello, C. Kiefer, A. P. LaGrow, L. Storozhuk, F. Perton, S. Begin, D. Mertz, N. T. K. Thanh and A. Gavriilidis, *Nanoscale*, 2021, **13**, 8795.
15 M. K. Jabali, A. R. Allafchian, S. A. H. Jalali, H. Shakeripour, R. Mohammadizezhad and F. Rahmani, *Colloids Surf., A*, 2022, **632**, 127743.
16 A. Criveanu, F. Dumitrache, C. Fleaca, L. Gavrila-Florescu, I. Lungu, I. P. Morjan, V. Socoliuc and G. Prodan, *Appl. Surf. Sci. Adv.*, 2023, **15**, 100405.
17 S. Kariminia, A. Shamsipur and M. Shamsipur, *J. Pharm. Biomed. Anal.*, 2016, **129**, 450.
18 L. Storozhuk, M. O. Besenhard, S. Mourdikoudis, A. P. LaGrow, M. R. Lees, L. D. Tung, A. Gavriilidis and N. T. K. Thanh, *ACS Appl. Mater. Interfaces*, 2021, **13**, 45870.
19 M. Theodosiou, E. Sakellis, N. Boukos, V. Kusigerski, B. Kalska-Szostho and E. Efthimiadou, *Sci. Rep.*, 2022, **12**, 8697.
20 E. P. McKiernan, C. Moloney, T. R. Chaudhuri, S. Clerkin, K. Behan, R. M. Straubinger, J. Crean and D. F. Brougham, *Acta Biomater.*, 2022, **152**, 393.
21 B. Özkahraman, E. Tamahkar, N. İdil, A. Kılıç-Suloglu and I. Perçin, *Drug Dev. Res.*, 2021, **82**, 241.
22 U.S. Food & Drug Administration, GRAS Notices Inventory, https://www.accessdata.fda.gov/scripts/fdcc/?set=GRASNotices (accessed 9 Nov 2025).
23 U.S. Food and Drug Administration, (n.d.). Inactive Ingredients Database (IID). U.S. Department of Health and Human Services. Retrieved, https://www.fda.gov/drugs/drug-approvals-and-databases/inactive-ingredients-database-download (accessed 9 Nov 2025).
24 M. Iv, N. Telischak, D. Feng, S. J. Holdsworth, K. W. Yeom and H. E. Daldrup-Link, *Nanomedicine*, 2015, **10**, 993.
25 L. Illum, *Pharm. Res.*, 1998, **15**, 1326.
26 D. Yan, Y. Li, Y. Liu, N. Li, X. Zhang and C. Yan, *Molecules*, 2021, **26**, 7136.
27 Q. Chen, C. Jia, Y. Xu, Z. Jiang, T. Hu, C. Li and X. Cheng, *Carbohydr. Polym.*, 2022, **290**, 119518.
28 S. Bhattacharjee, S. Goswami, S. Das, S. Bhattacharjee and S. Bhaladhare, *Mater. Today Commun.*, 2023, **36**, 106541.
29 Y. Nui, J. Wu, Y. Kang, P. Sun, Z. Xiao and D. Zhao, *Int. J. Biol. Macromol.*, 2023, **247**, 125722.
30 V. Manjusha, M. R. Rajeev and T. S. Anirudhan, *Int. J. Biol. Macromol.*, 2023, **235**, 123900.
31 I. O. Wulandari, D. J. D. H. Santjojo, R. A. Shobirin and A. Sabarudin, *Rasayan J. Chem.*, 2017, **10**, 1348.
32 S. Mahdi, H. Sahebi, H. Zandavar and S. Mirsadeghi, The design of experiment, *Composites, Part B*, 2019, **175**, 107130.
33 L. Wang, A. Hervault, P. Southern, O. Sandre, F. Couillaud and N. T. K. Thanh, *J. Mater. Chem. B*, 2020, **8**, 10527.
34 A. Hervault, A. E. Dunn, M. Lim, C. Boyer, D. Mott, S. Maenosono and N. T. K. Thanh, *Nanoscale*, 2016, **8**, 12152.
35 B. Joshi, U. Shankar, S. Vishwakarma, A. Kumar, A. Kumar, D. Joshi and A. Joshi, *ACS Appl. Bio Mater.*, 2023, **6**, 1943.
36 M. G. Adimoolan, N. Amreddy, M. R. Nalam and M. V. A. Sunkara, *J. Magn. Magn. Mater.*, 2018, **448**, 199.
37 M. Amirbandeh, A. Taheri-Kafrani, A. Soozanipour and C. Gaillard, *Biochem. Eng. J.*, 2017, **127**, 119.
38 S. Sadighian, K. Rostamizadeh, M. J. Hosseini, M. Hamidi and H. Hosseini-Monfared, *Toxicol. Lett.*, 2017, **278**, 18.
39 S. Sadighian, H. Monfared-Hosseini, K. Rostamizadeh and M. Hamidi, *Adv. Pharm. Bull.*, 2015, **5**, 115.
40 G. Bertotti, *Hysteresis in magnetism for physicist, material scientists, and eng*. Academic Press, San Diego, CA, 1998.
41 G. Unsoy, R. Khodadust, S. Yalcin, P. Mutlu and U. Gunduz, *Eur. J. Pharm. Sci.*, 2014, **62**, 243.
42 Y. Lou, Y. Li, J. Li, C. Fu, X. Yu and L. Wu, *RSC Adv.*, 2019, **9**, 10486.
43 E. S. Jang, Y. L. Seung, C. Eui-Joon, S. In-Cheol, K. C. Ick, K. Dukjoon, K. Young Il, K. Kwangmeyung and A. Cheol-Hee, *Pharm. Res.*, 2014, **31**, 3371.
44 M. Norouzi, V. Yathindranath, J. A. Thliveris, B. M. Kopec, T. J. Siahaan and D. W. Miller, *Sci. Rep.*, 2020, **10**, 11292.
45 M. Zare and M. N. Sarkati, *Polym. Adv. Technol.*, 2021, **32**, 4094.
46 Z. Yu, L. Ma, S. Ye, G. Li and M. Zhang, *Carbohydr. Polym.*, 2020, **236**, 115972.

47 S. M. Anush and B. Vishalakshi, *Int. J. Biol. Macromol.*, 2019, **133**, 1051.
48 M. Helmi and A. Hemmati, *Energy Convers. Manage.*, 2021, **248**, 114807.
49 E. F. Ribeiro, T. T. Barros-Alexandrino, O. B. G. Assis, A. Cruz, A. Quiles, I. Hernando and V. R. Nicoletti, *Carbohydr. Polym.*, 2020, **250**, 116878.
50 S. Moretto, A. S. Silva, J. L. D. Tuesta, F. F. Roman, R. Cortesi, A. R. Bertao, M. Banobre-Lopez, M. Pedrosa, A. M. T. Silva and H. T. Gomes, *Mater. Today Chem.*, 2023, **33**, 101748.
51 M. F. K. Ariffin and A. Idris, *Renewable Energy*, 2022, **185**, 1362–1375.
52 L. P. Nalluri, S. R. Popuri, C.-H. Lee and N. Terbish, *Int. J. Polym. Mater. Polym. Biomater.*, 2021, **70**, 1039.
53 X. Hai, L. Ma, Y. Zhu, Z. Yang, X. Li, M. Chen, M. Yuan, H. Xiong, Y. Gao, F. Shi and L. Wang, *Carbohydr. Polym.*, 2023, **321**, 121295.
54 G. R. Mahdavinia, H. Hoseinzadeh, P. Labib, P. Jabbari, A. Mohebbi, S. Barzeger and H. Jafari, *Polym. Bull.*, 2023, **80**, 12923.
55 S. R. Obireddy and W. F. Lai, *Int. J. Nanomed.*, 2022, **17**, 589–601.
56 S. M. A. Sadat, S. T. Jahan and A. Haddadi, *J. Biomater. Nanobiotechnol.*, 2016, **7**, 91.
57 S. D. Li and L. Huang, *Mol. Pharm.*, 2008, **5**, 496.
58 S. Mourdikoudis, R. M. Pallares and N.TK. Thanh, *Nanoscale*, 2018, **10**, 12871.
59 G. Yi, J. Ling, Y. Jiang, Y. Lu, L. Y. Yang and X. Ouyang, *J. Mol. Struct.*, 2022, **1268**, 133688.
60 S. W. Fatima, K. Imtiyaz, M. M. A. Rizvi and S. K. Khare, *RSC Adv.*, 2021, **11**, 34613.
61 N. Amiryaghoubi, E. D. Abdolahinia, A. Nakhlband, S. Asizad, M. Fathi, J. Barar and Y. Omidi, *Colloids Surf., B*, 2022, **220**, 112911.
62 M. Pourmadadi, S. Darvishan, M. Abdouss, F. Yazdian, A. Rahdar and A. M. Diez-Pascual, *Ind. Crops Prod.*, 2023, **197**, 116654.
63 S. U. D. Wani, M. Ali, M. H. Masoodi, N. A. Khan, M. I. Zargar, R. Hassan, S. A. Mir, S. P. Gautam, H. V. Gangadharappa and R. A. M. Osmani, *Vib. Spectrosc.*, 2022, **121**, 103407.
64 O. Veiseh, J. W. Gunn and M. Zhang, *Adv. Drug Delivery Rev.*, 2010, **62**, 284.
65 B. Lu, J. Wang, A. J. Hendriks and T. M. Nolte, *Environ. Sci.: Nano*, 2024, **11**, 406.
66 S. Shukla, V. Arora, A. Jadaun, J. Kumar, N. Singh and V. K. Jain, *Int. J. Nanomed.*, 2015, **10**, 4901.
67 S. Kazemi, M. Pourmadadi, F. Yazdian and A. Ghadami, *Int. J. Biol. Macromol.*, 2021, **186**, 554.
68 N. Pazouki, S. Irani, N. Olov, S. M. Atyabi and S. Bagheri-Khoulenjani, *Prog. Biomater.*, 2022, **11**, 43.
69 R. M. Patil, P. B. Shete, N. D. Thorat, S. V. Otari, K. C. Barick, A. Prasad and S. H. Pawar, *J. Magn. Magn. Mater.*, 2014, **355**, 22.
70 R. Fathi and R. Mohammadi, *Int. J. Biol. Macromol.*, 2023, **246**, 125546.
71 T. Wu, Y. He, L. Ding, F. Ding and F. Tan, *Inorg. Chim. Acta*, 2024, **559**, 121791.
72 B. D. Cardoso, V. F. Cardoso, S. Lanceros-Méndez and E. M. Castanheira, *Biomedicines*, 2022, **10**, 1207.
73 S. T. Haque, R. A. Islam, S. H. Gan and E. H. Chowdhury, *Int. J. Mol. Sci.*, 2020, **21**, 6721.
74 M. N. V. Ravi Kumar, *React. Funct. Polym.*, 2000, **46**(1), 1.
75 J. Berger, M. Reist, J. M. Mayer, O. Felt, N. A. Peppas and R. Gurny, *Eur. J. Pharm. Biopharm.*, 2004, **57**, 19.
76 I. A. Sogias, A. C. Williams and V. V. Khutoryanskiy, *Biomacromolecules*, 2008, **9**(7), 1837.
77 H. Zhang, M. Oh, C. Allen and E. Kumacheva, *Biomacromolecules*, 2004, **5**, 2461.
78 O. Helmi, F. Elshishiny and W. Mamdouh, *Int. J. Biol. Macromol.*, 2021, **184**, 325.
79 G. Lohiya and D. S. Katti, *Carbohydr. Polym.*, 2022, **277**, 118822.
80 V. Bakhshi, H. Poursadegh, M. S. Amini-Fazl, D. Salari and S. Javanbakht, *Polym. Bull.*, 2024, **81**, 7499.
81 H. H. Peng, D. X. Hong, Y. X. Guan and S. J. Yao, *Int. J. Pharm.*, 2019, **558**, 82.
82 S. Wilhelm, A. J. Tavares, Q. Dai, S. Ohta, J. Audet, H. F. Dvorak and W. C. Chan, *Nat. Rev. Mater.*, 2016, **1**, 16014.